Combined multi-modal photoacoustic tomography, optical coherence tomography (OCT) and OCT angiography system with an articulated probe for *in vivo* human skin structure and vasculature imaging

MENGYANG LIU,[1] ZHE CHEN,[1] BEHROOZ ZABIHIAN,[1] CHRISTOPH SINZ,[2] EDWARD ZHANG,[3] PAUL C. BEARD,[3] LAURIN GINNER,[1] ERICH HOOVER,[4] MICHEAL P. MINNEMAN,[4] RAINER A. LEITGEB,[1] HARALD KITTLER,[2] AND WOLFGANG DREXLER[1,*]

[1]*Center for Medical Physics and Biomedical Engineering, Medical University of Vienna, Währinger Gürtel 18-20, AKH 4L, Vienna, 1090, Austria*
[2]*Department of Dermatology, Medical University of Vienna, Währinger Gürtel 18-20, AKH 7J, Vienna, 1090, Austria*
[3]*Department of Medical Physics and Biomedical Engineering, University College London, Gower Street, London, WC1E 6BT, UK*
[4]*INSIGHT Photonic Solutions, Inc., 300 S. Public Road, Lafayette, CO, 80026, USA*
*wolfgang.drexler@meduniwien.ac.at

Abstract: Cutaneous blood flow accounts for approximately 5% of cardiac output in human and plays a key role in a number of a physiological and pathological processes. We show for the first time a multi-modal photoacoustic tomography (PAT), optical coherence tomography (OCT) and OCT angiography system with an articulated probe to extract human cutaneous vasculature *in vivo* in various skin regions. OCT angiography supplements the microvasculature which PAT alone is unable to provide. Co-registered volumes for vessel network is further embedded in the morphologic image provided by OCT. This multi-modal system is therefore demonstrated as a valuable tool for comprehensive non-invasive human skin vasculature and morphology imaging *in vivo*.

References and links

1. S. Standring, *Gray's Anatomy,* 41st ed. (Elsevier Limited, 2016).
2. M. Bhushan, H. S. Young, P. E. C. Brenchley, and C. E. M. Griffiths, "Recent advances in cutaneous angiogenesis," Br. J. Dermatol. **147**(3), 418–425 (2002).
3. D. F. Fiorentino, "Cutaneous vasculitis," J. Am. Acad. Dermatol. **48**(3), 311–344 (2003).
4. D. M. McDonald and P. L. Choyke, "Imaging of angiogenesis: from microscope to clinic," Nat. Med. **9**(6), 713–725 (2003).
5. S. H. Geyer, M. M. Nöhammer, I. E. Tinhofer, and W. J. Weninger, "The dermal arteries of the human thumb pad," J. Anat. **223**(6), 603–609 (2013).
6. S. H. Geyer, M. M. Nöhammer, M. Mathä, L. Reissig, I. E. Tinhofer, and W. J. Weninger, "High-Resolution Episcopic Microscopy (HREM): A Tool For Visualizing Skin Biopsies," Microsc. Microanal. **20**(5), 1356–1364 (2014).
7. D. Cosgrove, "Angiogenesis imaging--ultrasound," Br. J. Radiol. **76**(suppl_1), S43–S49 (2003).
8. C. Errico, J. Pierre, S. Pezet, Y. Desailly, Z. Lenkei, O. Couture, and M. Tanter, "Ultrafast ultrasound localization microscopy for deep super-resolution vascular imaging," Nature **527**(7579), 499–502 (2015).
9. S. Eriksson, J. Nilsson, and C. Sturesson, "Non-invasive imaging of microcirculation: a technology review," Med. Devices (Auckl.) **7**, 445–452 (2014).
10. L. Themstrup, J. Welzel, S. Ciardo, R. Kaestle, M. Ulrich, J. Holmes, R. Whitehead, E. C. Sattler, N. Kindermann, G. Pellacani, and G. B. E. Jemec, "Validation of Dynamic optical coherence tomography for non-invasive, in vivo microcirculation imaging of the skin," Microvasc. Res. **107**, 97–105 (2016).

11. A. Alex, B. Považay, B. Hofer, S. Popov, C. Glittenberg, S. Binder, and W. Drexler, "Multispectral in vivo three-dimensional optical coherence tomography of human skin," J. Biomed. Opt. **15**(2), 026025 (2010).
12. W. Drexler and J. G. Fujimoto, *Optical Coherence Tomography: Technology and Applications,* 2nd ed. (Springer International Publishing, 2015).
13. W. J. Choi, R. Reif, S. Yousefi, and R. K. Wang, "Improved microcirculation imaging of human skin in vivo using optical microangiography with a correlation mapping mask," J. Biomed. Opt. **19**(3), 036010 (2014).
14. U. Baran, Y. Li, W. J. Choi, G. Kalkan, and R. K. Wang, "High resolution imaging of acne lesion development and scarring in human facial skin using OCT-based microangiography," Lasers Surg. Med. **47**(3), 231–238 (2015).
15. C. Blatter, J. Weingast, A. Alex, B. Grajciar, W. Wieser, W. Drexler, R. Huber, and R. A. Leitgeb, "In situ structural and microangiographic assessment of human skin lesions with high-speed OCT," Biomed. Opt. Express **3**(10), 2636–2646 (2012).
16. B. Zabihian, J. Weingast, M. Liu, E. Zhang, P. Beard, H. Pehamberger, W. Drexler, and B. Hermann, "In vivo dual-modality photoacoustic and optical coherence tomography imaging of human dermatological pathologies," Biomed. Opt. Express **6**(9), 3163–3178 (2015).
17. W. Drexler, M. Liu, A. Kumar, T. Kamali, A. Unterhuber, and R. A. Leitgeb, "Optical coherence tomography today: speed, contrast, and multimodality," J. Biomed. Opt. **19**(7), 071412 (2014).
18. M. Liu, B. Maurer, B. Hermann, B. Zabihian, M. G. Sandrian, A. Unterhuber, B. Baumann, E. Z. Zhang, P. C. Beard, W. J. Weninger, and W. Drexler, "Dual modality optical coherence and whole-body photoacoustic tomography imaging of chick embryos in multiple development stages," Biomed. Opt. Express **5**(9), 3150–3159 (2014).
19. M. Liu, N. Schmitner, M. G. Sandrian, B. Zabihian, B. Hermann, W. Salvenmoser, D. Meyer, and W. Drexler, "In vivo three dimensional dual wavelength photoacoustic tomography imaging of the far red fluorescent protein E2-Crimson expressed in adult zebrafish," Biomed. Opt. Express **4**(10), 1846–1855 (2013).
20. Z. Chen, M. Liu, M. Minneman, L. Ginner, E. Hoover, H. Sattmann, J. Ensher, M. Bonesi, W. Drexler, and R. A. Leitgeb, "Phase-stable swept source OCT angiography in human skin using an akinetic source," Biomed. Opt. Express **7**(8), 3032–3048 (2016).
21. C. A. Schneider, W. S. Rasband, and K. W. Eliceiri, "NIH Image to ImageJ: 25 years of image analysis," Nat. Methods **9**(7), 671–675 (2012).
22. E. Zhang, J. Laufer, and P. Beard, "Backward-mode multiwavelength photoacoustic scanner using a planar Fabry-Perot polymer film ultrasound sensor for high-resolution three-dimensional imaging of biological tissues," Appl. Opt. **47**(4), 561–577 (2008).
23. B. E. Treeby and B. T. Cox, "k-Wave: MATLAB toolbox for the simulation and reconstruction of photoacoustic wave fields," J. Biomed. Opt. **15**(2), 021314 (2010).
24. H. Ding, J. Q. Lu, W. A. Wooden, P. J. Kragel, and X. H. Hu, "Refractive indices of human skin tissues at eight wavelengths and estimated dispersion relations between 300 and 1600 nm," Phys. Med. Biol. **51**(6), 1479–1489 (2006).
25. A. Lozzi, A. Agrawal, A. Boretsky, C. G. Welle, and D. X. Hammer, "Image quality metrics for optical coherence angiography," Biomed. Opt. Express **6**(7), 2435–2447 (2015).

1. Introduction

As the largest organ of the human body, skin is the site where many fundamental functions take place, such as immune surveillance, biochemical synthetic processes and body temperature regulation, etc [1]. About 5% of total blood flow goes to the skin to support all these functions, generating a complex blood vessel network inside the skin. This network consists of three plexus, namely the superficial plexus from which the capillary loops in the dermal papillae stem, the reticular dermal plexus which is mostly venous in the middle of the dermis and the deep dermal plexus that sits at the bottom or the undersurface of the reticular dermis. In addition to the step by step branching of blood vessels, thoroughfare channels and arteriovenous anastomosis are also found to modulate the microcirculation with the latter one being critical for thermoregulation [1]. Some other processes such as skin aging, cutaneous wound healing and skin grafting are also directly related to or affecting cutaneous vasculature.

Besides the above-mentioned functions and processes, blood vessels are directly or indirectly involved in most skin diseases including inflammatory and neoplastic diseases and skin malformations [2, 3]. Visualizing cutaneous blood vessel network is therefore important for a spectrum of studies from plastic and reconstructive surgeries where angiosome architecture is crucial for flap design and evaluation [1], to diagnosis and prognosis of various cutaneous diseases including neoplastic skin diseases for which prominent blood vessels are a clinical characteristic [2, 4]. From cadavers and isolated limbs, extracting the vasculature can

be achieved by ink injection studies, corrosion casts, dissection, radiography [1] or high resolution episcopic microscopy [5, 6], etc. But postmortem imaging inherently prohibits functional monitoring or longitudinal studies knowing that cutaneous vasculature sees constant physiological or pathological changes. Histological tissue sections also require a relatively long time for preparation before imaging. Intravital methods such as X-ray and computed tomographic angiography need ionization radiation and intravascular contrast agents. Their resolution is also not enough to resolve microvasculature. Micro magnetic resonance imaging and micro computed tomography have finer spatial resolution, but their application is mostly in preclinical studies, with micro computed tomography also having ionizing radiation exposure issues [4]. Using microbubbles as a contrast agent, color Doppler ultrasonography can demonstrate microcirculation in human, but it requires intravenous injection of inert gas [7, 8].

To overcome the limits seen by the current histological and clinical angiography methods in *in vivo* human skin vasculature imaging, alternative imaging methods have been explored extensively. Videomicroscopy technics, laser Doppler perfusion imaging and laser speckle contrast imaging (LSCI) have all been applied for non-invasive microcirculation studies [9], but none of them is capable of showing the whole skin vasculature in 3D knowing that the skin thickness can reach 5 mm depending on its location [1], let alone the lack of morphologic vessel resolvability in LSCI [10]. Optical coherence tomography (OCT) is claimed to provide human skin microstructural image up to 2 mm [10], which has a clinical diagnostic value in dermatology studies [11]. The functional extension of OCT angiography contrasts specifically blood flow against static tissue based on signal decorrelation without the need of contrast agents, thereby providing microvascular details with high contrast in strongly scattering tissue that are not visible with standard OCT [12]. OCT angiography has been applied to image facial or palmar human skin [13–15]. But even with focus field extension using Bessel beams or contrast enhancement algorithms to reduce the residual static artifacts, the effective angiographic imaging depth is well below 2 mm. Another optical imaging method, namely photoacoustic tomography (PAT), has been proven valuable to extract vasculature in humans. Various vessel patterns in both healthy and pathological palmar skin in human are demonstrated by PAT imaging [16]. Its penetration depth exceeds 5 mm, visualizing well the superficial vascular plexus and the reticular dermal plexus with even a hint of the deep dermal plexus. However, with 4 to 8 μm diameter for capillaries, 10 to 30 μm diameter for postcapillary venules [1], the resolution of PAT struggles to distinguish individual vessels in microvasculature. In addition to the resolution limits of PAT for microvasculature visualization, even though PAT has been demonstrated with good sensitivity for blood vessel detection, without spectroscopic extensions and multispectral processing algorithms, it cannot distinguish different types of absorbers. This means that when both melanin and hemoglobin are present in close proximity, which is the case in many regions in human skin, PAT alone cannot separate one from the other. OCT angiography, however, does not rely on absorption. As long as the decorrelation between B-scans passes the threshold set in the reconstruction algorithm, microvasculature can be resolved by OCT angiography. A dual modality PAT/OCT system with OCT angiography, then, could be a good solution.

Several combined PAT/OCT systems have been published in the past few years. But the use of scanned detectors or detection element arrays in PAT obstructs OCT A-scan acquisition [12]. Instead of using piezoelectric detectors for PAT, all optical PAT has been demonstrated to achieve satisfactory results when combined with either spectral domain OCT (SD-OCT) or swept source OCT (SS-OCT) [17]. Both preclinical results for *in toto* chick embryo imaging [18] and clinical skin disease imaging [16] have been shown, proving its usefulness in biomedical imaging. So far, however, in these dual modality PAT/OCT systems, the OCT part is only used to provide 1 to 2 mm of scattering based surface structural detail. The region imaged in clinics is also limited to only hand.

In this work, we demonstrate for the first time a multi-modal PAT/OCT system with OCT angiography function. The probing head of the system is mounted on an articulated arm for easy access to different parts of human body. The full cutaneous blood vessel network in different skin regions such as hand, arm, knee and foot is visualized by OCT angiography for the microvasculature and PAT for deeper plexus. 3D vasculature volumes from OCT angiography and PAT can be fused in transition zones where OCT angiography and PAT resolve the same vessels. Structural information of the skin is given simultaneously during OCT angiography scan, which allows visualization of the dermatoglyphics and the skin layers. Cutaneous wound healing and scarring in one subject's arm were also imaged using our multi-modal system. A comparison between darker and lighter skin is given, raising the discussion of the clinical feasibility of PAT for patients with different skin types.

2. Methods

We noticed that the Fabry-Perot interferometer (FPI) sensor used in our all optical PAT system for photoacoustic pulse detection, though permitting transmission of sample beam in the OCT system at a wavelength centered at 1060 nm, causes strong sensitivity loss for the OCT signal. The dielectric coating of the FPI induces phase changes in the OCT sample beam along with dispersion, which are hard to compensate. The passband limit of the FPI also makes OCT sources above 1200 nm not feasible for incorporation. Combining a 1300 nm OCT source is not achievable so we have to use two separate systems for imaging when this wavelength range is desired for OCT [19], which is not optimal for clinical translation. Knowing that most OCT dermatological research uses 1300 nm band for its good compromise between penetration depth and resolution [12], we designed a switchable sensor head for our dual modality PAT/OCT system so that the FPI sensor is only in place during PAT scan, while in the succeeding OCT scan another sensor head is placed to circumvent the passband limit and to avoid possible sensitivity drop from the FPI. With this switchable sensor head, we incorporated our latest phase stable SS-OCT angiography system featuring an akinetic source at 1340 nm [20] into the all optical PAT system. A probe for these two modalities is manufactured to be mounted on an articulated arm made from a boom stand (V7 Articulating Boom Stand, Omano Microscopes, China). A therapy bed (Therapieliege Jordan A1, Dr. Schuhfried Medizintechnik GmbH, Austria) was used in combination with the articulated arm so that all body regions can be reached. Figure 1(c) and Fig. 1(d) show the probe in working mode in addition to 3D modeling effects given by Fig. 1(a) and Fig. 1(b) (Solid Edge ST6, Siemens Industry Software GmbH, Germany).
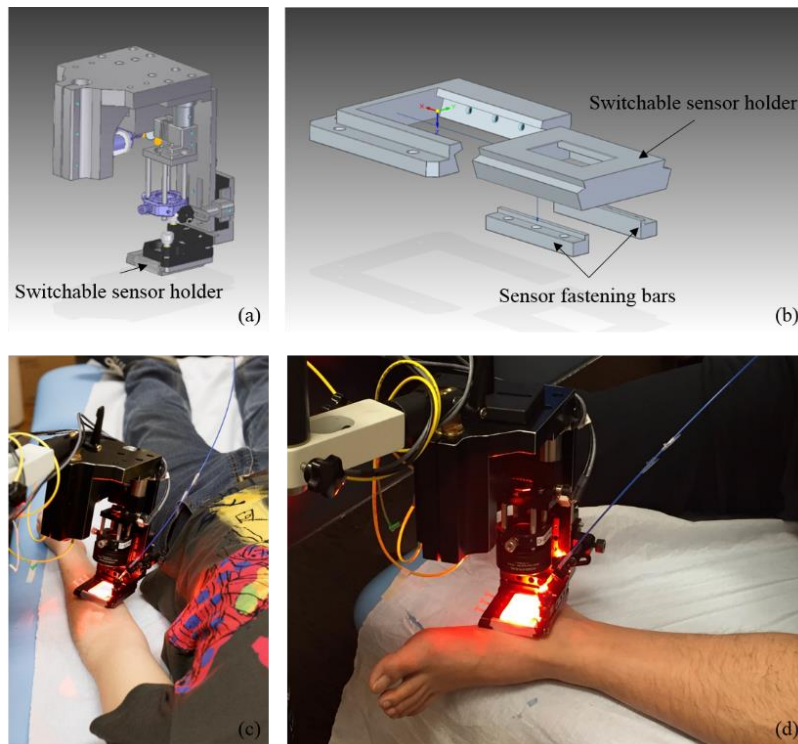
Fig. 1. (a) 3D modeling of the multi-modal system's scanning probe. (b) An exploded view of the switchable sensor holder assembly. (c) The probe in PAT scan imaging an arm. (d) The probe in PAT scan imaging a foot.

Compared to other all optical PAT/OCT systems' configurations [16, 18], this newly designed probe has all degrees of freedom to be positioned pertaining to the regions being imaged. The switchable sensor holder slides in and out of the slot easily, permitting fast removing and changing of sensor holder to allow OCT a clear scanning window without FPI. The excitation fiber clamp (VH1/M, Thorlabs, US) is mounted to a z-axis translation stage (MT1/M, Thorlabs, US) to which the sensor holder unit is bolted, meaning that the fluence onto the sample does not change during sensor height adjustment, enhancing repeatability of results. To reduce the probe size, we changed the previous design and employed a pair of galvanometer mirrors (6210H, Cambridge Technology, US) in close proximity. For clinical imaging, we still use a sequential imaging manner: human subjects will lie in the bed or be seated; clear image gel (05-812, NEXT Medical Products Company, US) is then applied to the region to be imaged; the articulated probe pushes against the region being imaged and gentle pressure is exerted to squeeze out the air bubbles trapped in between the skin and the sensor surface; PAT scan is performed over a region of 12 mm $\times$ 12 mm using an excitation wavelength of 610 nm at a pulse repetition rate of 50 Hz with a pulse width $<$ 3 ns (VersaScan/BB/HE, GWU-Lasertechnik Vertriebsges.mbH, Germany) and an estimated optical fluence on skin surface of 4 mJ/cm^2, so chosen due to FPI's passband limit and laser safety requirements; after about 8 minutes the PAT will finish its interrogation laser (Tunics T100S-HP-CL, Yenista Optics, France) scan with a step size of 80 μm; while the PAT data is being pre-processed and saved, the FPI sensor holder is slid off the sensor holder unit and the OCT sensor holder slides in position, with a transparent cover glass replacing the FPI; OCT scans are performed with each B-scan being scanned four times consecutively for OCT angiography. The OCT scan also covers a range of 12 mm $\times$ 12 mm with 512 A-lines and 512 B-scans (512 $\times$ 512 detection points). The incident power measured on skin is about 6.2 mW.

Running the swept source (SLE-101, INSIGHT Photonic Solutions, Inc., US) at 200 kHz sweep rate, the total imaging time for OCT is within 10 seconds. The swept source features an all semiconductor design and thus requires no extra phase stabilization. Phase sensitivity is guaranteed by its linearity and sweep phase repeatability. A schematic of the PAT/OCT system is given in Fig. 2.
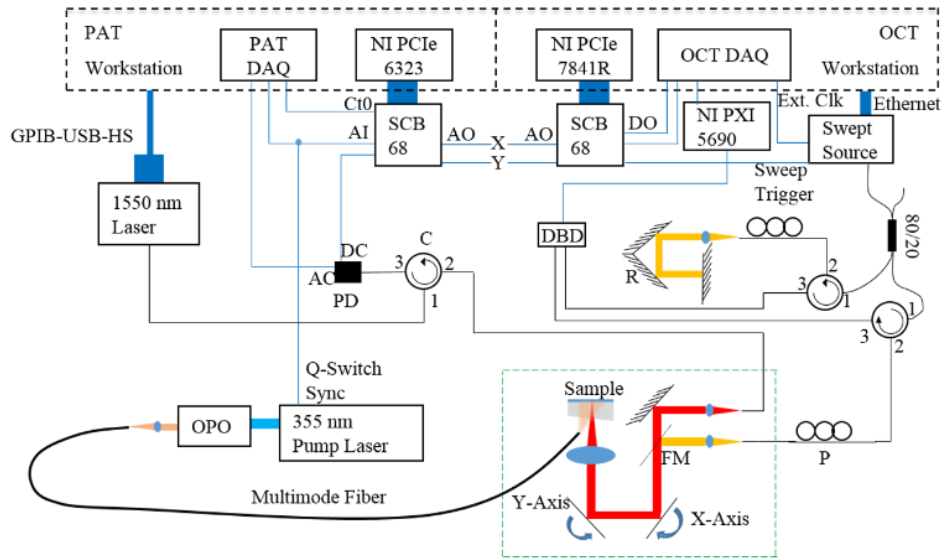

Fig. 2. Schematic of the multi-modal system. The green dashed line encircles the probe. Black dashed line indicates the two workstations used for PAT and OCT. The two sub-systems share the same probe. DO: digital output; AO: analog output; Ct: counter; AI: analog input; OPO: optical parametric oscillator; DAQ: data acquisition card; Ext. Clk: external clock; R: retroreflector; C: circulator; P: polarization controllers; FM: flip mirror; DBD: dual balanced detector; PD: photodetector.

The output from the excitation fiber (FT1500EMT, Thorlabs, US) delivers the visible beam onto the sample. Absorbers inside skin convert the optical energy to photoacoustic pulses, whose backward propagation induces deformation of the FPI, which is in turn detected by the reflectivity change of the interrogation laser beam, whose wavelength is set to the optimum bias point for each point scanned on the sensor. The back reflected PAT probing beam goes through a circulator (6015-3-FC, Thorlabs, US) and the intensity change is converted and amplified in a homemade transimpedance amplifier before being acquired by a data acquisition device (NI PCI-5114, National Instruments, US). For the OCT part, output from the swept source goes through an 80:20 fiber coupler (CP-S-P-2 $\times$ 2-131-20/80-900-1-1-FA, Laser Components Ltd, UK) to divide the beam into the sample and the reference arms. Same circulators (CIR-1310-50-APC, Thorlabs, US) and polarization controllers (FPC030, Thorlabs, US) are used in both arms as well as matched fibers. A dual balanced detector (096214, INSIGHT Photonic Solutions, Inc., US) relays the interference signal to a preamplifier (NI PXI-5690, National Instruments, US) before it is acquired by a data acquisition device (ATS9360, AlazarTech, Canada) which is externally clocked by the swept source. The data acquisitions are trigger by the pump laser (Quanta-Ray Pro270-50, Spectra-Physics, US) and the swept source for PAT and OCT, respectively. Synchronization between data acquisition and scanning is achieved using a multifunction data acquisition card (NI PCIe-6323, National Instruments, US) for PAT and a field-programmable gate array (NI PCIe-7841R, National Instruments, US) for OCT. The interrogation laser and the swept

source also communicate with the workstations through a GPIB controller for Hi-Speed USB (NI GPIB-USB-HS, National Instruments, US) and an Ethernet cable, respectively. The control applications for the multi-modal system are programmed in LabVIEW (LabVIEW 2015, National Instruments, US). Post-processing and image reconstruction are done using MATLAB (MATLAB 2015b, MathWorks, US). Volume rendering and animation are achieved using ImageJ [21] and Amira (FEI, France). As for a more detailed description of the working principles of all optical PAT and akinetic SS-OCT as well as the algorithms used for image reconstruction and enhancement, the readers are referred to [12, 22, 23] and [20], respectively.

Several human subjects are imaged using our multi-modal PAT/OCT/OCT-angiography system for skin regions of hand, arm, knee and foot. For hand and arm imaging the subjects sit in a patient chair while the probe presses from above. For knee and foot imaging the subjects lie or sit in the therapy bed while the probe approaches from aside. During imaging, the subjects are required to wear laser protection goggles (R01.S1759.1001, LASERVISION GmbH & Co. KG, Germany). All procedures are approved by the Ethics Committee of the Medical University of Vienna and the European Union Medical Device Directive. The OCT morphology volume and the OCT angiography volume are inherently co-registered in that they arise from the same data set. Since there is a sensor holder switching procedure between the PAT and OCT scans, careful registration among the PAT, OCT and OCT angiography volumes is performed using the transition zone in which OCT angiography and PAT resolve the same blood vessels or the matched skin creases visualized in PAT and OCT. By manually tweaking one modality's projected image against the other modality's projected image in an expanded canvas, a good overlay can be achieved. The two volumes are cropped accordingly to generate co-registered volumes. These volumes are then resliced and resampled to share the same voxel dimension. Finally, these volumes are loaded into different channels for 3D rendering and animation.

Using an achromatic doublet (AC508-075-C, Thorlabs, US) as the scan lens, we characterized the system by imaging a 1951 USAF target (57-898, Edmund Optics, US). The lateral resolutions are 75.3 µm and 54.6 µm for PAT and OCT, respectively. The axial resolutions are 30.8 µm for PAT and 26.6 µm in air for OCT. All resolution values are experimentally measured. A sharp edge from the USAF target in reconstructed images in the central field of view (FOV) is selected to calculate the edge spread function (ESF). Line spread function (LSF) is then computed by taking the derivative of the ESF. After Gaussian curve fitting for the LSF, the full width at half maximum (FWHM) values are used as the respective lateral resolutions for OCT and PAT. Since the thickness of the chrome coating on the target is one order of magnitude smaller than the axial resolutions of OCT and PAT, plots in the depth dimension through the coated part of the target in the reconstructed images are used to calculate the respective axial resolutions. The FWHM values of the Gaussian fitted curves in the axial direction are taken as the axial resolutions. Taking 1.43 as the refractive index for epidermis [24], the axial resolution of OCT is 18.6 µm in tissue. Sensitivity of the OCT sub-system is measured to be 103 dB, which approaches the shot noise limit.

3. Results

Figure 3 shows the results from a right knee. Figure 3(a) gives a 3D view of the PAT results. The small bright dots on top are the eccrine glands. Figure 3(b), which is shown in the same 3D orientation as Fig. 3(a), displays the OCT morphology volume, whose top surface demonstrates the secondary creases in triangular areas. The lower left corner of Fig. 3(b) is a photo of the knee imaged with a dashed square indicating the approximate region scanned. Figure 3(c) and Fig. 3(d) are fused OCT angiography and PAT *en face* view images. Green denotes PAT signals and red maps OCT angiography data. We can see from Fig. 3(c) that a bright-pigmented layer is visible in green, bearing the skin surface pattern lines given in Fig. 3(b). Co-registration of the PAT and OCT volumes in this case is achieved by matching the

skin crease patterns in Fig. 3(c).We assume the signals generated in this layer is from the melanin in basal cell layer in the epidermis. Summing 49 µm from 403 µm beneath the cornified layer, we saw the blood vessel network mostly given by OCT angiography in Fig. 3(d). The bright lines in Fig. 3(d) could be caused by pixel-to-pixel shifts in the B-scans [25]. PAT does not reveal many vessels in this depth range presumably due to its lack of sensitivity for detecting smaller vessels with less absorbers. Figure 3(e) is a maximum intensity projection (MIP) image of PAT, confirming that the epidermis has a strong absorption layer. In the corner of Fig. 3(e), some vellus hairs are also visualized as tortuous lines. Eccrine gland orifices are also visible in Fig. 3(e) as approximately equidistant bright dots dispersed over the image. Figure 3(f) shows deeper vessels visualized in PAT. For Fig. 3(f), a modified hue saturation value (HSV) coordinate is used, where hue is projected to reflect different depths and value is mapped to intensity. For sake of simplicity, saturation in these MIP images is set to be always 1 in the HSV coordinate. The hue to depth projection is given by the color bars to the right of Fig. 3(f). The same type of HSV coordinate is also used for Fig. 4, Fig. 5 and Fig. 6. Negative vignette is observed in Fig. 3(e) and Fig. 3(f). This is due to the geometric mismatch of the scan lens's focal plane to the flat surface of the FPI sensor used for PAT.
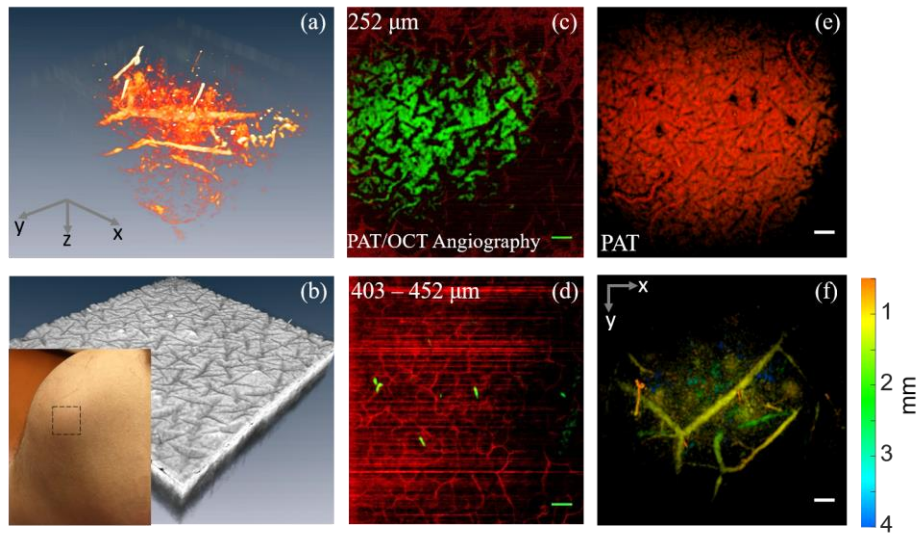

Fig. 3. (a) 3D display of PAT resolved blood vessels. (b) OCT morphologic volume showing the skin creases. The inlet is a photo of the knee imaged with the dashed square indicating approximately the scanned region. (c) A slice in the dermal-epidermal junction giving PAT in green and OCT angiography in red. (d) Summation of the depth range from 403 to 452 µm for the fused PAT and OCT angiography volume. PAT in green and OCT angiography in red. (e) An MIP image of PAT showing the strong absorbing layer before reaching reticular dermis. (f) An MIP image of PAT with hue to depth projection, visualizing deeper vessels in the skin of knee. Scale bar = 1 mm.

As is shown in Fig. 1(d), we also imaged the cutaneous vasculature of a foot. The results are given below in Fig. 4.
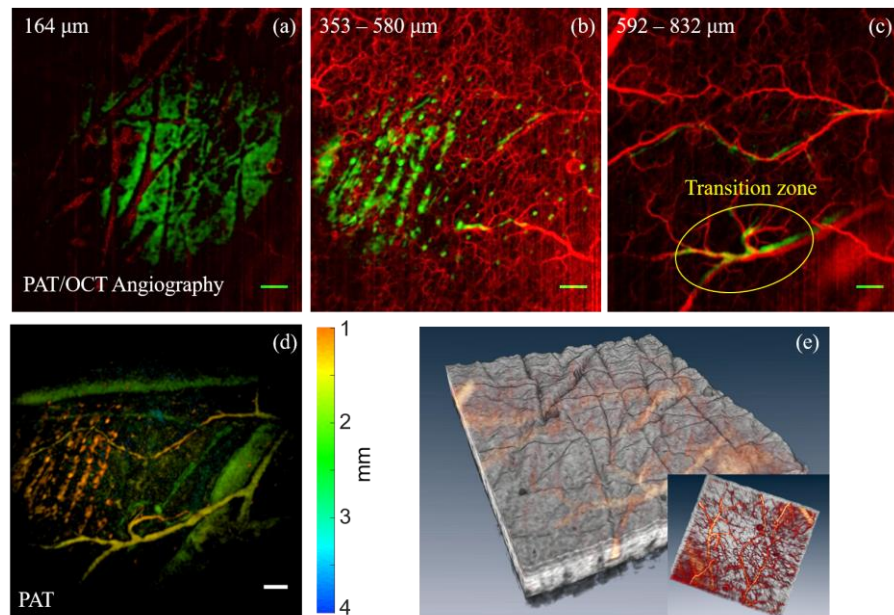
Fig. 4. (a), (b) and (c) are from the fused PAT/OCT-angiography volume with green for PAT and red for OCT angiography. (a) A slice at 164 μm measured from the surface of the skin. (b) Summation for the depth range between 353 μm and 580 μm. (c) Summation from 592 μm to 832 μm. (d) PAT MIP image in HSV coordinate with depth to hue projection showing a depth range of 3 mm from 1 mm below skin surface. (e) 3D snapshots of fused PAT/OCT and OCT angiography volume (see Visualization 1). Gray color maps OCT while red hot color map is used for blood vessels from OCT angiography and PAT. Scale bar = 1 mm.

Similar as in Fig. 3(c), we can see from Fig. 4(a) an absorption layer at the papillary dermis, presumably attributing to the melanin concentration in the dermal-epidermal junction. In Fig. 4(b), intertwined microvasculature network is visualized by OCT angiography while absorption contrast is given by PAT in green. Eccrine glands are visible, as in Fig. 3(a), as small dots along some parallel absorption lines. We speculate that the PAT signals in Fig. 4(b), as well as the orange hued signals in the left part of Fig. 4(d), are a result from both melanin and hemoglobin. This speculation roots from the parallel appearance of the lines that follow the skin fringes. We believe that the undulating dermal-epidermal junction, which can be seen from Visualization 1, generates this pattern. When integrating in depth involving this junction and displaying the integrated image *en face*, regions covering more of the dermis will have stronger signal while regions with more of the epidermis have smaller or no signal. Because in the junction both capillary loops and melanocytes can be found, while PAT does not have a fine enough resolution to differentiate hemoglobin from melanin in this application, we assume this pattern can be attributed to both absorbers. The slightly structurally indented eccrine gland and the capillary network surrounding its root contribute to the dotted appearance in the figures. At the far limit of OCT angiography's penetration depth, PAT carries on to visualize vessels in deeper depth range. In Fig. 4(c), the yellow line circles the region where overlapped blood vessels are found in PAT and OCT angiography. This depth range marks the effective imaging depth of OCT angiography, meaning that from 832 μm and beneath, it will be PAT to visualize the reticular plexus. Figure 4(d) gives the PAT MIP image with HSV coordinate and hue to depth projection from 1 mm to 4 mm. OCT morphology volume demonstrates the skin's detailed structure in Fig. 4(e), where primary, secondary and tertiary skin creases can be discerned as well as the junction between epidermis and dermis. Both Fig. 4(e) and its inlet show the vasculature seen through the

morphological volume. A video is provided for Fig. 4(e) to better demonstrate the fused data set with PAT, OCT and OCT angiography.
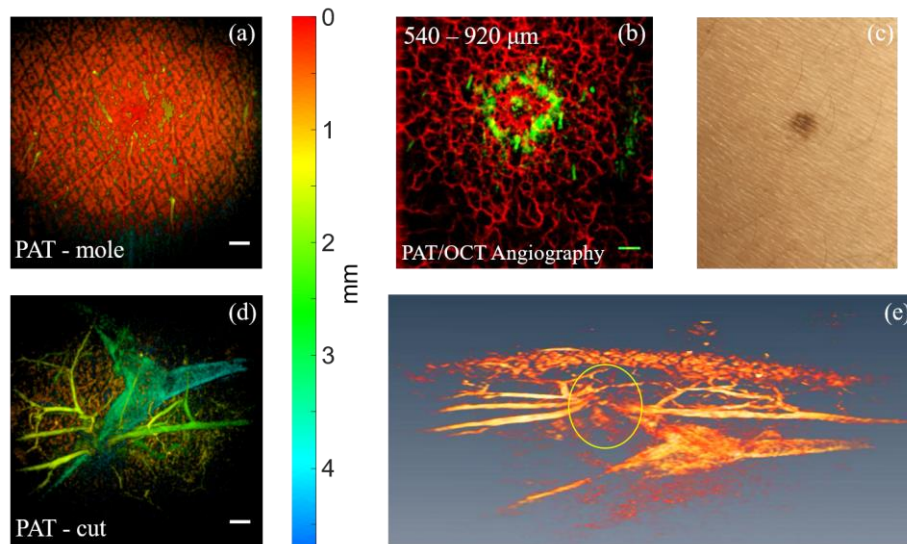

Fig. 5. (a) PAT MIP image of type III skin over a depth of 4.6 mm. (b) PAT/OCT-angiography image over a depth range of 380 μm from 540 μm below skin surface with red for OCT angiography resolved blood vessels and green for PAT signal. (c) A photo of the nevus imaged in type III skin. (d) PAT MIP image of type II skin in the arm over a depth of 4.6 mm. The hue to depth projection bar to the right of (a) and (d) means that these two figures share the same projection. (e) 3D display of (d), showing the ruptured blood vessels (inside the yellow circle) and granulation tissue caused by a wound in the arm. Scale bar = 1 mm.

Figure 5 shows the results for imaging two arms of different skin types (by Fitzpatrick scale). Figure 5(c) is a photo of a melanocytic nevus in a lower arm in an individual with skin type III (white to light brown). Figure 5(a) is an MIP image over 4.6 mm depth from skin surface of PAT imaging the nevus in Fig. 5(c). Figure 5(b) shows the summation over the depth range from 540 μm to 920 μm with fused PAT and OCT angiography. Figure 5(d) gives a PAT MIP image also over 4.6 mm for an arm with skin type II (white). A newly healed wound is in the middle of the FOV, which is better demonstrated by the circled zone in Fig. 5(e), whose 3D rendering shows the ruptured blood vessels torn upwards towards skin surface. A hue to depth projection bar is given to the right of Fig. 5(a) and Fig. 5(d), indicating that these two figures use the same projection for consistency. Comparing Fig. 5(a) and Fig. 5(d), we find astonishingly that the strong absorption layer in skin type III fully blocks the blood vessel visualization below in the MIP image, while in skin type II, deep dermal plexus can be seen with a thick vessel seated at a depth about 4.6 mm from skin surface.

Figure 3, Fig. 4 and Fig. 5 are in the regions of hairy skin. Figure 6 demonstrates the results we acquired imaging glabrous skin of the palm. Figure 6(a) to Fig. 6(c) show blood vessels from PAT/OCT-angiography fused volumes in increasing depths. In Fig. 6(a), we can notice that small capillary loops originating from the superficial plexus are visualized to be distributed along the ridges of the palmar skin. This means that the smallest vessel units are discernable from OCT angiography imaging. Figure 6(b) shows the blood vessel network over about 290 μm. In Fig. 6(c), we find the transition zone again, with both PAT (in green) and OCT angiography (in red) showing the same sets of vessels. Fusing the vessel network from OCT angiography and PAT using the transition zone, we can generate a 3D display of cutaneous vasculature which is demonstrated in Fig. 6(d). The flattened surface in Fig. 6(d) is caused by pressing a cover glass in the OCT sensor holder against the skin. Blood vessels in

deeper plexus visualized by PAT branch off stage by stage to support the microcirculation in the superficial plexus which is extracted from OCT angiography. Figure 6(e) and Fig. 6(f) show PAT MIP images over different depth ranges with HSV coordinates. Comparing Fig. 6(a) with Fig. 6(e) we notice that PAT cannot resolve capillary and postcapillary venules in skin due to resolution limit, but hemoglobin and melanin together will generate stripes in PAT MIP images. In Fig. 6(f) we see that PAT is, however, capable of imaging deep seated vessels covering the whole thickness of skin. Figure 6(g), also Fig. 6(d), are snapshots of a video showing 3D rendering of the fused PAT/OCT/OCT-angiography data.
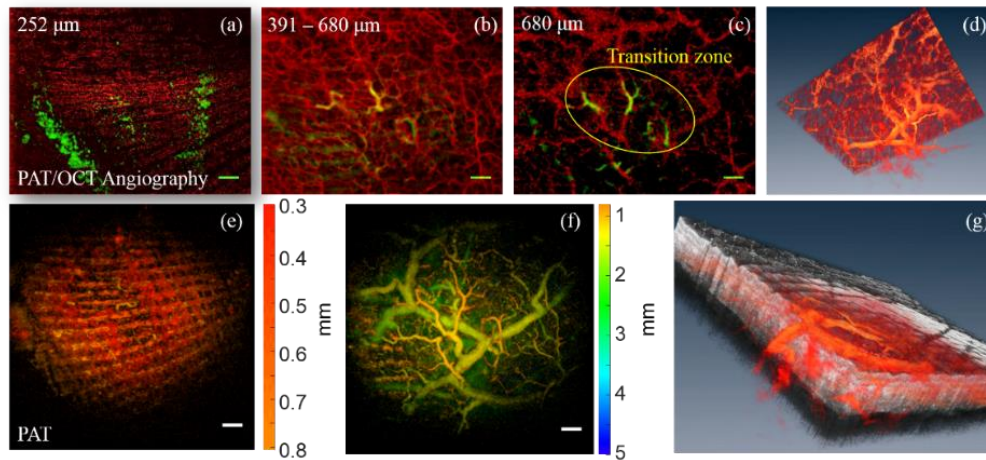

Fig. 6. (a), (b) and (c) are fused PAT/OCT-angiography images with PAT in the green channel and OCT angiography in the red channel. (a) A slice at 252 μm below skin surface. Capillary loops are visible following the ridges. (b) Summation over the depth range from 391 μm to 680 μm. Postcapillary venules are displayed using OCT angiography. (c) A single slice at 680 μm into skin shows where the transition zone from OCT angiography to PAT locates. (d) Whole cutaneous blood vessel network given in volumetric display by fused OCT angiography and PAT data. (e) PAT MIP image with HSV coordinate. Same pattern is observed as is given in (a) but capillary loops not distinguishable. (f) PAT MIP image in deeper region showing blood vessels located in and below reticular dermis. (g) A snapshot of the 3D volume with OCT in gray, OCT angiography and PAT in red color map (see Visualization 2). Scale bar = 1 mm.

4. Discussion

The PAT/OCT system with OCT angiography extension has the advantage of comprehensively mapping the full cutaneous blood vessel network *in vivo* in human. Although the lateral resolution of the OCT sub-system is 54.6 μm, which is larger than the diameter of capillary and some arterioles and venules, microvasculature is still successfully resolved. This is due to the fact that as long as there is phase variation in consecutive B-scans, the reconstructed pixel can reflect such difference even if the capillary's dimension is smaller than the pixel size. However, densely packed capillary loops in tissue could cause issues for OCT angiography to visualize small vessels. In PAT, we noticed that the current FOV cannot reach the extent of the scanned region, suffering from a strong negative vignette. Both issues request a customized scan lens. A single achromatic doublet, although 2 inch in aperture, still distorts the focal plane of the telecom wavelength interrogation laser. Although with the switchable sensor holder design OCT does not suffer from reduced effective FOV, the lateral resolution is almost twice its theoretical value. We plan to customize a scan lens for both 1310 nm and 1550 nm, which are about the central wavelengths for the SS-OCT system and the PAT interrogation laser, respectively. Disparities in their focal planes arising from wavelength differences can be partially compensated by the z-axis translation stage to which the sensor holders are mounted.

The substrate of the FPI sensor has a certain angle to the Fabry-Perot cavity. This angle slightly deflects the interrogation laser beam. In OCT and OCT angiography, we also intentionally induce an angle for the cover glass which is glued to the OCT sensor head. For optimal signal to noise ratio (SNR), these two angles are different. During the sensor holder switching process, the sensor holder unit gets detached with the scanned region. After switching it is pushed against the skin again. This procedure causes slight differences in skin thickness. Even though proper co-registration between PAT and OCT can be achieved using the skin creases – basal layer absorption matching and the OCT angiography – PAT blood vessel transition zone, an accurate merging of the three data sets in 3D is still challenging when the error needs to be limited within couple tens of micrometers, especially in the depth dimension. A proper automatic volume matching algorithm needs to be developed using the two levels of matching information to accurately and quickly merge PAT, OCT and OCT angiography data sets. Another issue is that OCT angiography's SNR decreases rapidly in depth. Although vessels beyond 800 μm below skin surface can also be resolved by OCT angiography, it is a challenge to properly render these vessels in 3D due to increased noise introduced by multiply scattered light. With this in mind, in Fig. 4 and Fig. 6, as soon as the blood vessel transition zone is detected, we crop off deeper slices in the OCT angiography volume. Though this gives better 3D visualization effect, less overlapped vessels between OCT angiography and PAT are used for volume co-registration. We plan to investigate OCT angiography noise reduction and vessel filter algorithms to enhance the transition zone's depth range for a more accurate co-registration between each modality's volumes.

Skin type differences turn out to be a limiting factor for the applicability of the multi-modal PAT/OCT/OCT-angiography system in clinical settings. For the same optical fluence incident upon the skin, less pigmented skin permits deeper penetration depth while darker skin tones get most of the excitation energy absorbed in the pigmented layer before the laser pulse reaches deep seated vessels. Although OCT angiography's penetration depth is not limited by skin type, transition zone becomes inconspicuous for type III skin. With 4 mJ/cm^2 fluence at 50 Hz repetition rate, we do not have much room to go for increasing the fluence. What we can do, though, is to reduce the repetition rate of the excitation source to allow higher fluence on the skin. Therefore, we plan to run the excitation laser at different repetition rates for different skin types, in the hope of achieving similar penetration depth in PAT, even though this means that for darker skin tones the data acquisition time may be increased several folds. We also plan to recruit volunteers of all skin types to test our multi-modal system to quantify how melanin concentration affects PAT's effective imaging depth. The relatively long data acquisition time in PAT is largely due to the 50 Hz repetition rate of the excitation source. An excitation source with higher repetition rate could significantly reduce the imaging acquisition time.

In Fig. 3(e) and Fig. 4(d), eccrine glands are visible in PAT. Per the excitation wavelength used, it is not very likely that the absorption of 610 nm light pulses by sweat can contribute significantly to the photoacoustic signal, knowing that water absorption at 610 nm is low. The authors assume that the prominent appearance of these sweat glands in PAT could be attributed to the slightly denser vascular network distribution around the glands. But this phenomenon requires a more careful investigation in the future to explain.

The articulation of the current boom stand cannot be precisely adjusted, making gradual increments difficult to control, while this is necessary between sensor holder switching. During imaging, the therapy bed does not have any fixation accessories. This renders a high requirement for the human subject's compliance. Some subjects were not able to stay stable over a complete imaging session. To solve these issues, we have modified our design of the probe. In the second generation design, a portable rack is used in combination with the therapy bed, which is also mobile. All degrees of freedom for positioning the articulated probe are enabled by using a series of articulates that are mounted to the rack. Finer and repeatable positioning can be realized by translation stages customized for the rack. Vacuum

pads are also implemented in the second generation system for securing and fixing the subjects' imaged body parts during scanning. We are further investigating new polymer film sensor designs which have minimized effects on the OCT system's sensitivity in the hope of eliminating the sensor switching procedure and hence the possibility for simultaneous multi-modal scanning.

5. Conclusion

A dual modality PAT/OCT system with OCT angiography extension is demonstrated to comprehensively image human skin *in vivo*. Several different parts of the body and two skin types are tested using this system, showing its ability to visualize the full cutaneous vasculature non-invasively. The microvasculature revealed by OCT angiography is succeeded in depth by a visualization of its feeding blood vessel network visualized by PAT. OCT, at the same time, provides a structural background for OCT angiography and PAT. Large imaging area and deep penetration depth are achieved by fusing the volumetric data sets from OCT, PAT and OCT angiography matching transition zones or skin creases. To the authors' knowledge, this is the first method for intravital non-invasive full cutaneous vasculature imaging in human from capillary loops to arteries and veins. It makes a diagnostically powerful and quite interesting tool for morphological blood vessel imaging, which could have a strong impact for studies requiring angiosome, angiogenesis or vasculature malformation information. In addition to its potentials in anatomy, dermatology and reconstructive surgery, with spectroscopic extensions, this multi-modal system can also be applied in functional studies to understand physiological and pathological processes.